Materials Science & Engineering A 809 (2021) 140869

Contents lists available at ScienceDirect

Materials Science & Engineering A

journal homepage: http://www.elsevier.com/locate/msea

Effect of grain orientation on the compressive response of highly oriented MAX phase Ti_3SiC_2

Xingyuan Zhao [a], Maxim Sokol [b], Michel W. Barsoum [b], Leslie Lamberson [a,*]

[a] Department of Mechanical Engineering, Colorado School of Mines, CO, 80401, USA
[b] Department of Materials Science and Engineering, Drexel University, Philadelphia, PA, 19104, USA

ARTICLE INFO

Keywords:
MAX phase
Compression
Titanium silicon carbide
Highly oriented
Rate sensitivity

ABSTRACT

The MAX phases comprise of a group of layered ternary carbides that exhibit unique mechanical properties which bridge the gap between their metal and ceramic constituents. To study the effects of the global grain orientation, Ti, Si and TiC powders were hot pressed to synthesize highly oriented bulk Ti_3SiC_2. X-ray diffraction (XRD) was used to verify the grain orientation and a Lotgering factor of 0.87 with respect to the c-axis was obtained. Prepared Ti_3SiC_2 samples have been compressed in two orientations, loading along the c-axis (‖c-axis) and perpendicular to the c-axis (⊥c-axis) at 10^{-3} s^{-1} using a standard load frame and at 10^{2} s^{-1} using a Kolsky (split-Hopkinson) bar. The average compressive strength along the ⊥c-axis orientation was 761 MPa under quasi-static conditions and 987 MPa under dynamic loading, exhibiting a 30% increase on average. The ‖c-axis orientation exhibited no rate dependence in compressive strength; however both orientations exhibited an increase of strain at failure under dynamic conditions by over 0.5%, on average. The orientation-dependent failure behavior at different strain rates were examined using high-speed imaging and 2D digital image correlation (DIC) during loading and via scanning electron microscopy (SEM) post-mortem. Results indicate that the ⊥c-axis fracture surface exhibited a mixture of transgranular and intergranular cracks, kink bands and delaminations, whereas ‖c-axis was limited to a combination of intergranular and transgranular cracks. Such fracture distinctions due to the availability (or lack thereof) for kink band formation appear to be responsible for the anisotropic compressive behavior.

1. Introduction

MAX phases are 3D layered solids comprising of early transition metals (M), A group elements (A), and carbides and nitrides (X). They have plate-like grains with unit structures of M_4AX_3, M_3AX_2 and M_2AX compositions [1,2]. This type of material combines some of the desirable proprieties of metals and ceramics such as machinability, resistance to thermal shock, high stiffness and an advantageous strength and toughness combination [3–6]. The weaker metallic bonding between A element atoms and other (M and X) atoms in the complex hexagonal structure allows only limited basal slip at ambient temperatures.

It has long been assumed that the deformation mechanisms of MAX phases were predominantly formation, slip and multiplication of basal plane dislocations that can be arranged into pileups or walls [7–12]. Recent studies made the case that ripplocations, which represent atomic scale buckling, are the operative deformation mechanisms in layered, crystalline solids, including MAX phases [13–17]. Kink bands, resulting from irrecoverable buckling upon further loading of ripplocations, were observed, especially when the basal planes were loaded edge-on [11]. Consequently, ripplocations explain the micromechanism in the elastic region prior to the formation of kink bands and eventual permanent failure in the material under load. In addition to kink bands, MAX phases can also deform by delaminations (or splits between layers), void formation and grain boundary sliding [4,8,18,19]. Under quasi-static conditions, the strain-stress hysteresis response of MAX phases has been shown to be reproducible, and essentially fully recoverable after the first loading cycle [8,20,21]. As such, ripplocation formations demonstrate a quasi-plastic, pseudo-ductile behavior under global compression (and local compression-shear) that results in potentially improved damage accommodation [8,20,22–25]. The hexagonal crystal structure and nanolayered microstructure contributes to the anisotropic properties; however, most prior studies have focused on randomly oriented bulk MAX phases due to the difficulty of texturing ceramics [26].

Texture-engineered ceramics have attracted recent attention due to

* Corresponding author.
E-mail address: les@mines.edu (L. Lamberson).

https://doi.org/10.1016/j.msea.2021.140869
Received 21 August 2020; Received in revised form 23 January 2021; Accepted 29 January 2021
Available online 17 February 2021

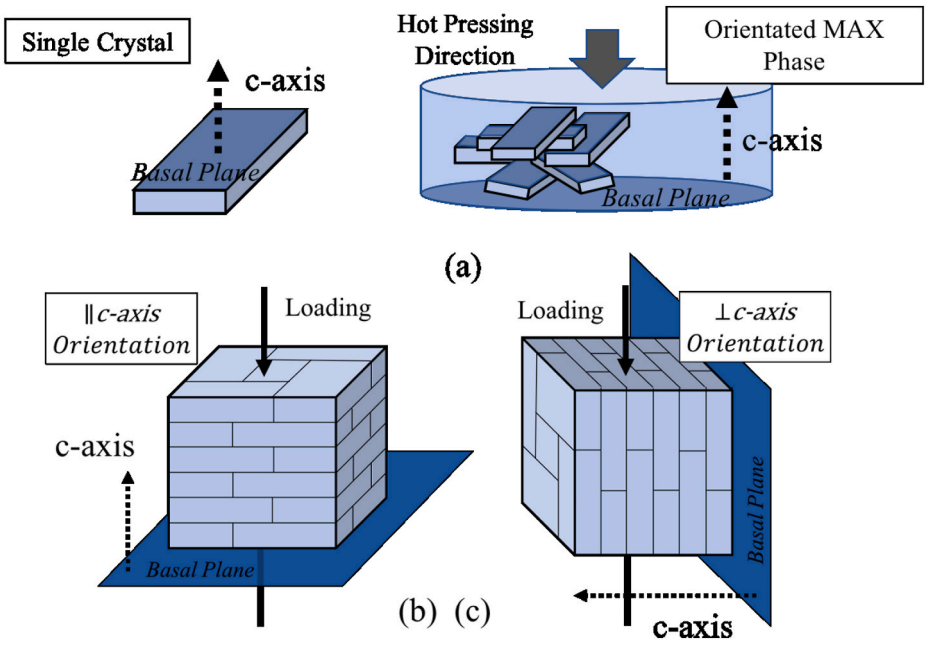

Fig. 1. Schematic of grain orientations. (a) A single crystal MAX grain and a stack of MAX phase grains aligned along the c-axis during hot pressing. (b) Simplified schematic of ∥c-axis loading orientation. (c) Simplified schematic of ⊥c-axis edge-on orientation.

their ability to produce property enhancements through crystallographic tailoring [27,28]. By altering the intrinsic crystallographic and extrinsic microstructural characteristics, textured ceramics can exhibit anisotropic properties like single crystals, as well as the robust mechanical ability to tailor a wide range of compositions like their bulk ceramic variants [27]. The term texture describes the global non-random crystallographic orientation of the grains. The simplest indicator for texture that can be calculated is the Lotgering factor ranging from 0 to 1, where 0 is random orientation and 1 is perfect orientation. The factor, $f_{(00l)}$, is calculated from the intensities of the X-ray diffraction (XRD) peaks under 2θ scan mode [29,30].

In MAX phases, grains prefer to grow along the basal plane to form a platelet shape [27]. Oriented MAX phase grains have a globally aligned texture axis, the c-axis, but are randomly aligned perpendicular to the c-axis. Fig. 1(a) illustrates a simplified single crystal MAX grain and how hot pressing aligns the grains. Recent studies on textured MAX phases include: texturing Cr_2AlC by spark plasma sintering [31], Nb_4AlC_3 by slip casting under a strong magnetic field [32–34], Ti_2AlC by hot pressing [35] and spark plasma sintering [36], Ti_2AlN by spark plasma sintering [37], Ti_3AlC_2 by spark plasma sintering [38,39] and slip casting under a strong magnetic field [40], and Ti_3SiC_2 by slip casting under a strong magnetic field [41,42], electrophoretic deposition [43] and spark plasma sintering [36]. The textured Ti_3SiC_2, Ti_2AlC and Ti_3AlC_2 reported the Lotgering factor $f_{(00l)}$ between 0.51 and 0.69 and a moderate improvement of mechanical properties including fracture toughness, electrical and thermal conductivities [36,38]. Texturing processed by slip casting under a magnetic field with the Lotgering factor $f_{(00l)}$ between 0.95 and 1 exhibited the most significant property improvements [34,41,42]. In the case of Ti_3AlC_2, both flexural strength and fracture toughness in the perpendicular and parallel to the orientation direction were improved relative to randomly oriented samples. The reported flexural strength for randomly orientated, perpendicular to the orientation direction and parallel to the orientation direction of Ti_3AlC_2 samples were 320 MPa, 1005 MPa, and 1261 MPa, respectively. The fracture toughness values of the aforementioned orientations were reported as 6.9 MPa $\sqrt{m}$, 14.6 MPa$\sqrt{m}$, and 13.1 MPa$\sqrt{m}$, respectively [40]. Note that these studies were under quasi-static loading.

There is relatively little research focused on the dynamic behavior of the MAX phases [44–49], and the dynamic compressive response of highly-oriented MAX phases, to the author's knowledge, has not been previously reported. At the same time, the unique combination of the properties in MAX phases and their noted damage tolerance make them potential candidates for applications involving impact and complex loading scenarios. Specifically, Ti_3SiC_2 exhibits relatively high stability and fracture toughness at high temperatures, high electrical and thermal conductivities, as well as a moderate resistance to oxidation, making this particular MAX phase a promising candidate for aircraft and diesel engine applications [1,4], to name a few.

Herein we define two experimental orientations: ∥c-axis means loading along the texture orientation c-axis as shown in Fig. 1(b), and ⊥c-axis means loading perpendicular to the c-axis as shown in Fig. 1(c). In this investigation, we characterize the compressive response of fully dense, hot pressed, highly-oriented Ti_3SiC_2 with ∥c-axis and ⊥c-axis orientations at quasi-static and dynamic strain rates. In addition, a Vickers hardness test and microscopy is performed to complement the rate and orientation-dependent compressive strength assessment.

2. Method

2.1. Material fabrication and characterization

Dense textured polycrystalline Ti_3SiC_2 bulk samples were prepared by ball milling a 1:1:1.05 stoichiometric mixture of TiC (325 mesh, 99%, Alfa Aesar), Si (325 mesh, 99.5%, Alfa Aesar), and Ti (325 mesh, 99%, Alfa Aesar) powders for 12 h in a polyethylene jar using zirconia milling balls. The mixed powders were loaded into a 1.5 in circular graphite die, coated with boron nitride and densified in a hot press, with graphite heating elements and a vacuum of < 10 Pa. The initial sintering conditions were as follows: a peak temperature of 1250°C, heating rate of 400°C/h, uniaxial pressure of about 10 MPa and a dwell time of 2 h. After cooling, the obtained samples were 73% dense. This porous preform was then loaded into a larger 2.5 in circular graphite die for further densification. The die was then heated at a rate of 400°C/h, to a maximum temperature of 1450°C. After reaching the maximum temperature, a uniaxial load corresponding to a stress of 40 MPa was applied and maintained for 4 h before cooling.

The compositions and grain orientation of the top (∥c-axis) and cross-section (⊥c-axis) surfaces of the sintered sample (see Fig. 1(b and c))

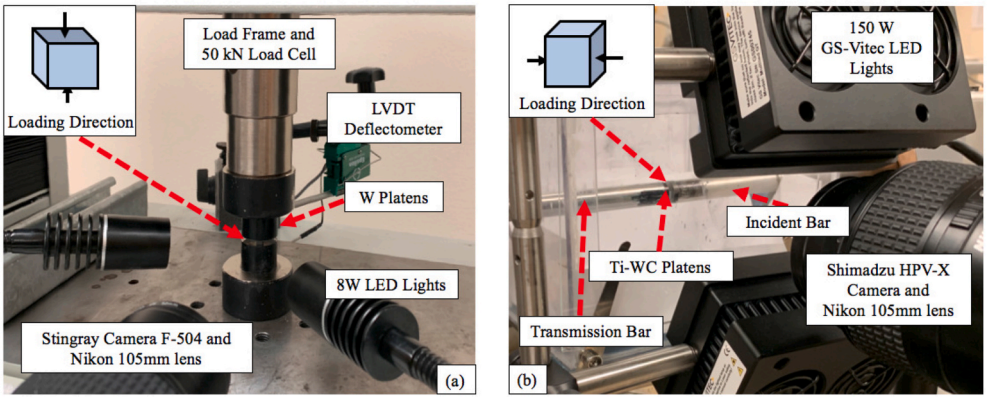

Fig. 2. Experimental setups for (a) quasi-static and (b) dynamic compression experiments.

were examined using a diffractometer (Rigaku SmartLab, Tokyo, Japan) with a 10 mm slit and a Cu tube. The scans were performed over the range of 5°–70° 2θ, with a step size of 0.02° and a dwell time of 0.5 s per step. Once the orientation was confirmed, the Lotgering orientation factor, f_L=(P–P_0)/(1-P_0), was calculated from the XRD patterns. For the *a b*-axis orientation of the hexagonal structure, P and P_0 were obtained from the ratio of $\sum I_{(hk0)}/\sum I_{(hkl)}$, and for the c-axis orientation, P and P_0 were calculated from the ratio of $\sum I_{(00l)}/\sum I_{(hkl)}$. Here $\sum I_{(hkl)}$, $\sum I_{(hk0)}$ and $\sum I_{(00l)}$ are the sum of peak intensities of the corresponding (*hkl*), (*hk*0), and (00*l*) planes on the 2θ diffractogram.

For microstructure analysis, the sample was mounted, ground, polished and etched for 2–3 s by a 1:1:1 part solution of hydrofluoric acid (48%, Sigma Aldrich, St. Louis, MO), nitric acid (68%, Alfa Aesar, Ward Hill, MA) and water. The samples were analyzed using a scanning electron microscope, SEM (XL30, FEI, Hillsboro, OR). The SEM images were processed using ImageJ software to obtain the average grain size [50]. Additional pre- and post-failure secondary and/ or backscattered electron SEM micrographs were taken with a Zeiss Supra 50VP and a FEI XL30 SEM to observe the microstructure and deformation mechanisms. Vickers hardness (Riehle Hardness machine) was tested at 20 N with a dwell time of 10 s.

2.2. Experimental methods

Specimens sized 5 × 5 × 5 mm^3 were cut from the same billet using electrical discharge machining (EDM) method for both quasi-static and dynamic experiments. EDM helped achieve parallelism of sample sides and the surfaces parallel to the base of billet were carefully marked and tracked during the sample preparation and experiments. Additionally, XRD was used to verify the orientation of samples. The orientations regarding the loading are illustrated in Fig. 1(b) for ∥c-axis and (c) for ⊥c-axis. Note that Ti_3SiC_2 grains are oriented around the c-axis, but are randomly oriented perpendicular to it. Prior to the experiments, all specimens were polished to a 3 μm surface finish on the loading surfaces and to a 15 μm surface finish on all other surfaces using an Allied TechPrep Polishing machine. A subset of the specimens were painted with a black and white speckle pattern using an airbrush in order to utilize 2D digital image correlation (DIC) measurements. Another subset of specimens were kept polished (and unpainted) in order to better observe the surface crack nucleation and propagation once damage is initiated during loading.

DIC is a non-contact, in-situ full-field optical technique that measures surface displacement and deformation where a series of images is taken of specimens with random and high contrast patterns during loading [51,52]. Tracking features of the pattern between the image from an undeformed specimen and comparing it with images taken during deformation allows for the strain field on the specimen surface to be obtained. The position of a small group of pixels (subset) is compared with the reference still-image for every deformed image and a local displacement is determined. Such determination is repeated in the field of view once every step size for a good sampling of data to map the full-field displacement. The strain measured using DIC method is only reliable before reaching catastrophic failure due to the one-to-one correspondence correlation requirement (which does not traditionally account for a free surface). It should be noted that the surface pattern quality (contrast, size, randomness, etc.) affects the accuracy of the strain measurement, particularly during high strain-rate loading where ultra high-speed imaging devices lack high pixel resolution [53]. For this study, commercially available DIC software, MatchID, was utilized for the strain mapping and the subset and step size were determined by conducting a performance analysis. Relevant DIC parameters are listed in Table 3.

Quasi-static compressive experiments were performed to obtain the low strain rate compression baseline at 0.5 mm/min to a nominal strain rate of 1.67 $\times 10^{-3}$ s^{-1}. Specimens were tested using a Shimadzu AG-IS load frame, placed in between two tungsten carbide platens attached to the load cell using a small amount of vacuum grease. A small amount of molybdenum disulfide powder was applied to the specimen surfaces to minimize the friction between the sample and the platens. The load frame had a 50 kN load cell with an Epsilon LVDT deflectometer. A Stingray F-504 camera (2452 x 2056 pixel) with a Nikon 105 mm lens and 8 W LED lights were used for imaging. The quasi-static experimental configuration is shown in Fig. 2(a).

A Kolsky (or split-Hopkinson pressure) bar was used to determine material properties at high strain rates based on the stress-wave propagation within the system [54]. The experimental setup included a 3 m long incident bar, a 3 m long transmission bar, and a 129 mm striker bar. All bars were made of C-350 maraging steel, with a diameter of 12.7 mm and an ultimate tensile strength of 2 GPa. A pneumatic pressure system propeled the striker into the incident bar at a known velocity to generate and propagate a compressive stress wave pulse. Specimens were sandwiched in between the two long bars with Ti jacketed WC platens of the same diameter as the Kolsky bars. The platens were approximately 3 mm thick, placed in alignment with the Kolsky bar using a small amount of vacuum grease. The platens were polished to a 15 μm surface finish on the side in contact with the Kolsky bar and to a 3 μm surface finish on the side in contact with the specimen.

When the stress wave traveling at the elastic wave speed reaches the specimen-bar interface, a portion of the incident pulse passes through the specimen and gets transmitted to the transmission bar while a small portion of the incident pulse is reflected back to the incident bar. The strain gauges located on the incident bar measure the incident strain pulse (ε_I) and reflected strain pulse (ε_R), and the strain gauge on the transmission bar records the transmitted strain pulse (ε_T). To extend the loading pulse, a 3 mm diameter, 1.2 mm thick copper pulse shaper was placed on the striker contact face at the incident bar [55]. Once the

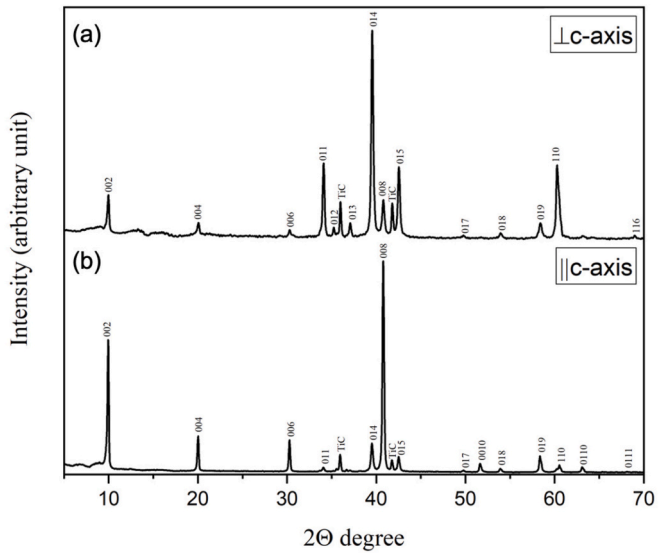

Fig. 3. XRD scans of (a) cross-section (⊥c-axis), and (b) top (||c-axis) surfaces.

Table 1
Material Properties of highly-oriented Ti_3SiC_2.

Density	Grain Size	Porosity	Orientation
g/ cm^3	μm	%	
4.5± 0.1	26±7	<1	$f_{(00l)}$ =0.87, $f_{(hk0)}$=0.31

one-dimensional elastic stress state is achieved in the specimen, the strain rate, strain, and stress are given by:

$$\dot{\boldsymbol{\varepsilon}}(t) = -2\frac{c_b}{L_s}\varepsilon_R(t) \tag{1}$$

$$\boldsymbol{\varepsilon}(t) = \int_0^t \dot{\varepsilon}(\tau)d\tau \tag{2}$$

$$\boldsymbol{\sigma}(t) = \frac{A_b E_b}{A_s}\varepsilon_T(t) \tag{3}$$

where $\dot{\varepsilon}(t)$ is the strain rate, $\varepsilon_R(t)$ is obtained from the reflected wave-pulse measured by the strain gauge on the incident bar, c_b is the bar longitudinal wave speed, A_b is the bar area, E_b is the bar elastic modulus, A_s is the specimen impact area and L_s is the specimen length. More details on these experiments can be found in Ref. [56]. For this study, 103 kPa (or 15 psi) gas pressure was used to attain a striker velocity of approximately 18 m/s, resulting in strain rates between 600 s^{-1} to 900 s^{-1}. A Shimadzu HPV-X ultra-high speed camera (400 x 250 pixel) at 2 M frames per second with a 150 mm Nikon lens and150 W GS Vitec MultiLED QT lights were used for imaging. The Kolsky setup is shown in Fig. 2(b).

3. Results and discussion

3.1. Orientation and material properties

Fig. 3 shows the XRD patterns of the textured bulk Ti_3SiC_2 billet in two orientations: the cross-section of puck-shape billet (⊥c-axis orientation) and the top surface of the same billet (||c-axis orientation). The oriented sample was relatively phase pure with only 4.1 wt% of TiC as a minor secondary phase impurity. The density was 4.5±0.1 g/cm^3, and was considered fully dense with a porosity of <1% (undetectable with Archimedes methods) as listed in Table 1. By comparing the XRD patterns of the scanned surfaces (⊥c-axis vs. ||c-axis), a strong change in the intensities can be observed due to preferred crystallographic orientations. After analyzing the difference between the relative intensities of the various diffracting peaks, it was found that all strong reflections belong to 00*l* planes in the top surface, meaning that the c-axis of the grains is perpendicular to the top surface. On the other hand, for the cross-section surface, most of the non-basal diffraction peaks 0*kl* have much higher intensities than the basal peaks 00*l*. The XRD results indicate that the Ti_3SiC_2 grains are oriented and have a global texture orientation c-axis, similar to the texture orientation found in previous work on MAX phases. The calculated Lotgering orientation factors confirm the oriented structure of the Ti_3SiC_2 sample: for the oriented top surface, $f_{(00l)}$ was determined to be 0.87, and for the oriented cross-section surface, $f_{(hk0)}$ was determined to be 0.31.

The SEM images revealed the plate-shape elongated cross-section of Ti_3SiC_2 basal planes in the cross-section (⊥c-axis) in Fig. 4(a), and relatively equiaxed grains with only basal planes observed, that are perpendicular to the c-axis (||c-axis) in Fig. 4(b). The average grain size, determined from the SEM images, was found to be approximately 26±7 μm (Fig. 4). The Vickers hardness of ⊥c-axis and ||c-axis have a value of 3.7±0.1 and 4.4±0.3 GPa, respectively. The indentation impression in Fig. 5(a) show an isotropic square shape for ⊥c-axis orientation with delaminations, intergranular cracks and transgranular cracks around the edges. In Fig. 5(b), the ||c-axis has a more elongated rhombus indentation shape with cracks only parallel to the basal planes spreading in one direction on the surface. Similar ||c-axis crack propagation can be found in Refs. [32,38], but the observed ⊥c-axis deformation was not as anisotropic as [31,32,37–39]. The ||c-axis hardness value is 19% higher than the value of ⊥c-axis. It is clear that under quasi-static compression conditions, delaminating the basal planes is easier than penetrating into them parallel to the c-axis. Such anisotropic indentation fracture behavior was also previously reported in other textured MAX phases [32,37,38,40,41], with similar higher hardness value on ||c-axis

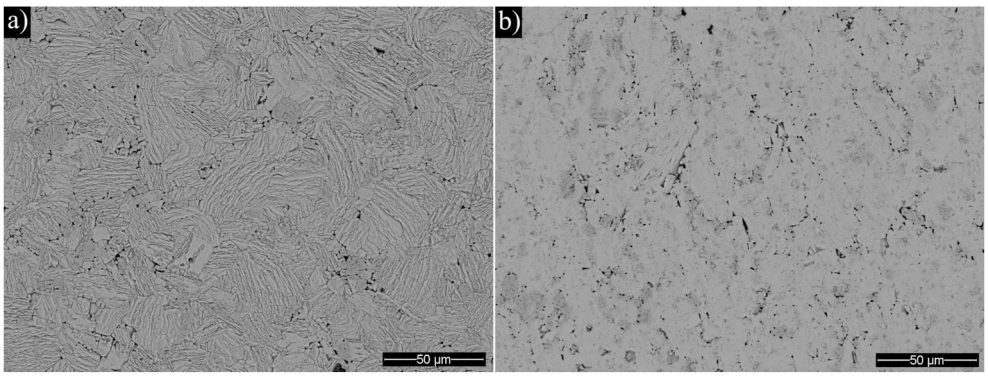

Fig. 4. SEM micrographs of (a) cross-section (⊥c-axis), and (b) top surface (||c-axis).

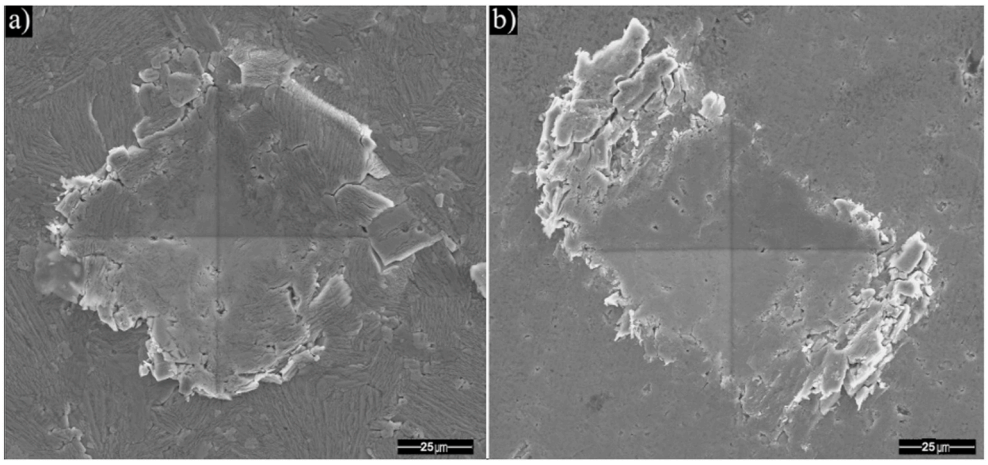

Fig. 5. SEM micrographs of Vickers hardness indentations into (a) cross-section (⊥c-axis), and (b) top surface (‖c-axis).

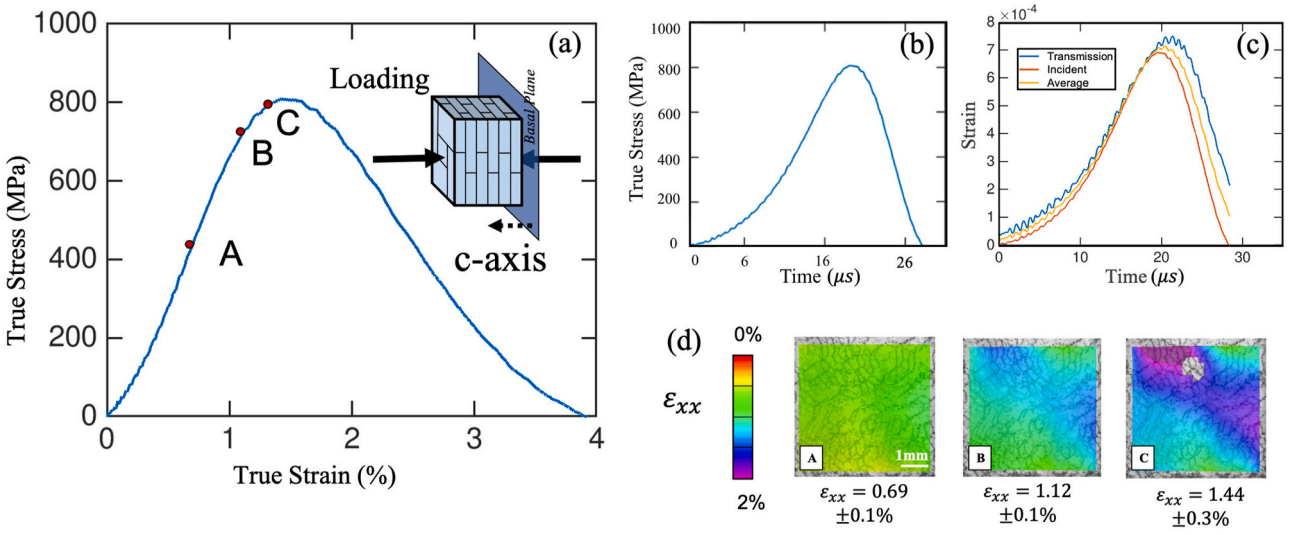

Fig. 6. Characteristic result of highly oriented Ti_3SiC_2 under dynamic compression. (a) True stress versus true strain in the ‖c-axis orientation. (b) True stress versus time of the same sample. (c) Dynamic force equilibrium of the strain gauge readings from incident bar, transmission bar, and the average versus time. (d) Representative average surface DIC maps for various points during loading showing axial strain in the *x* or horizontal loading direction.

orientation [32,37,40,41], except for [38] which reported a higher hardness value on ⊥c-axis orientation.

3.2. Quasi-static and dynamic behavior

A characteristic result of Ti_3SiC_2 under dynamic compression ‖c-axis is shown in Fig. 6. For this study, failure is defined as the peak compressive stress the specimen sustained. The stress-strain curve in Fig. 6(a) indicates that this specimen reached a peak stress of 814 MPa at a strain value of approximately 1.51%. The stress-time curve is shown in Fig. 6(b). The equilibrium of the strain reading on the transmission and incident gauges, as well as the average of those two readings are plotted against time in Fig. 6(c). The DIC surface axial strain analysis at three points during loading is shown in Fig. 6(d). On average, the DIC measurements were in agreement with the strain values obtained from the strain gauges shown in Fig. 6(a). The full-field strain spectrum illustrates that larger deformation took place in the diagonal direction across the specimen where at point C, right before the specimen failed, a 45° crack appeared. Correlation was lost there due to the appearance of the crack interrupting the one-to-one correspondence of surface pattern.

At least four specimens were tested to obtain an average in the two orientations and two strain rates examined and the results are summarized in Table 2. The DIC parameters utilized in the full-field strain analysis are listed in Table 3. The parameters were chosen for a robust, least biased correlation result. The strain rate against the peak compressive stress is plotted in Fig. 7. On average, the dynamic compression achieved a strain rate of 750 ± 140 s^{-1} in the ⊥c-axis orientation and 680 ± 80 s^{-1} in the ‖c-axis orientation. The ⊥c-axis specimens failed at a peak average stress of 987 MPa under dynamic conditions and only 761 MPa under quasi-static conditions, showing clear rate sensitivity. Conversely, the ‖c-axis orientation exhibited no sensitivity in peak compressive stress.

Table 2
Hardness and compressive response of highly oriented Ti_3SiC_2.

Orientation	Hardness [GPa]	Strain Rate [s^{-1}]	Peak Stress [MPa]	Peak Strain %
⊥c-axis	3.7 ± 0.1	1.7×10^{-3}	761 ± 38	0.55 ± 0.08
		$7.5 \times 10^{2} \pm 140$	987 ± 88	1.39 ± 0.28
‖c-axis	4.4 ± 0.3	1.7×10^{-3}	792 ± 30	0.76 ± 0.07
		$6.8 \times 10^{2} \pm 80$	782 ± 45	1.34 ± 0.32

Table 3
DIC parameters used for the 2D deformation analysis of highly oriented Ti_3SiC_2 under compression.

DIC Parameters	Quasi-static	Dynamic
Pre-filtering	Gaussian	Gaussian
Subset	35	12
Step size	12	5
Correlation criterion	ZNSSD [60]	ZNSSD [60]
Shape Function	Affine	Affine
Interpolation function	Bicubic Spline	Bicubic Spline
Pixel to mm conversion	150	28

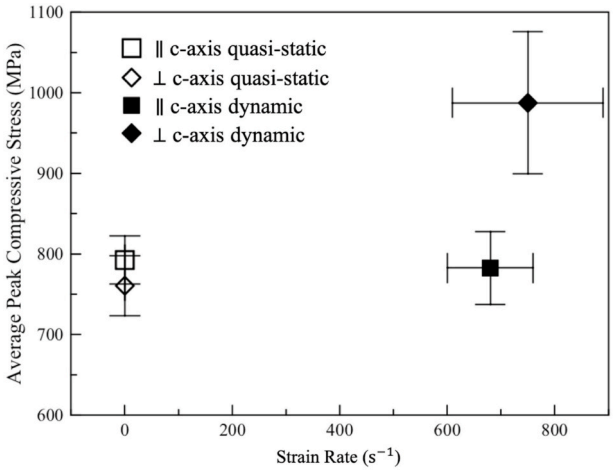

Fig. 7. Plot of resulting compressive stress versus strain rate on highly oriented Ti_3SiC_2.

Interestingly, both orientations exhibited an increase in strain at failure under dynamic conditions, although the reasons for this increase are not fully understood. In the structural ceramics community (e.g. AlN and SiC), it has been suggested that the increase in strain at failure under dynamic conditions exhibited is associated with potential activation of dislocation motion, or essentially these materials may exhibit some flow under high pressures [57,58]. Moreover, natural layered materials have also been shown to increase strain at failure under dynamic conditions compared to quasi-static. For example in nacre, the strain to failure shift has been reasoned to coincide with fracture being dominantly intergranular propagation under quasi-static loading, shifting to transgranular under dynamic loading [59]. Thus a competition or essentially the zigzag fashion of the failure path (competing between trans- and inter-) may cause the noted improvement, and a similar shifting of fracture patterning could potentially play a role here.

Comparing results within the same strain rate, under quasi-static conditions there was no obvious change in peak compressive stress between the two orientations with only 4% difference on average and overlapped standard deviation. Under dynamic conditions, both orientations failed at similar strains, but the ⊥c-axis failed at a peak stress 26% higher than the ‖c-axis. It should be noted that peak compressive stress of randomly oriented Ti_3SiC_2 has been shown to range from 560 to 935 MPa with similar grain sizes compared to this work [9,19,25] and thus all the results on highly oriented variants (within their standard deviation) fall within this range. Overall, these findings do highlight some clear rate sensitivity, as well as the anisotropic behavior in Ti_3SiC_2.

To better understand the different failure behavior, we turn our attention to the surface fracture patterns observed via imaging. In Fig. 8, images of a ⊥c-axis and a ‖c-axis experiment are shown in reference to their corresponding position on the stress-strain curve. The ‖c-axis (red line) has a peak stress of 711 MPa and 0.93% strain at failure. As the stress builds up, dominant cracks propagated along the diagonal direction of the sample (as shown in Fig. 8(b)). Shortly after the peak stress, the specimen initially fractured at approximately 45° (macroscopically) and splintered into smaller chunks and fragments. The ⊥c-axis shown in Fig. 8(a) (black line) was imaged parallel to the c-axis, i.e. the imaging surface was mainly comprised of basal planes. The characteristic result showed a peak stress of 1073 MPa and 1.09% strain at failure. The associated high-speed images in Fig. 8(c) captured a more graceful fracture behavior than the ‖c-axis, where the specimen comminuted on itself. As a result, macroscopic cracks on the basal plane surface were rarely visible in the high-speed images. Powderized Ti_3SiC_2 clouds coming from the specimens were also observed. For this orientation, cracks predominantly existed along the basal planes, as evident in the larger plate-shape like fragments post-mortem. Occasionally, out-of-plane cracks were observed, but were not dominant like in the ‖c-axis orientation.

Characteristic results of quasi-static compression along the two orientations are shown in Fig. 9. The majority of the specimens in both orientations did not separate completely into individual fragments after reaching peak stress suggesting quasi-brittle behavior. The ‖c-axis specimen response increased linearly nearly until failure at 763 MPa and 0.70% strain. Images captured angled shear like crack formation as shown in Fig. 9(b), and in this case the sample fractured into three dominant fragments. While this angled fracture behavior was similar to the dynamic ‖ c-axis failure, the quasi-static cases resulted in far fewer fragments. Similar approximate 45° (relative to the loading axis) crack behavior has been observed in randomly oriented dynamic [46] and

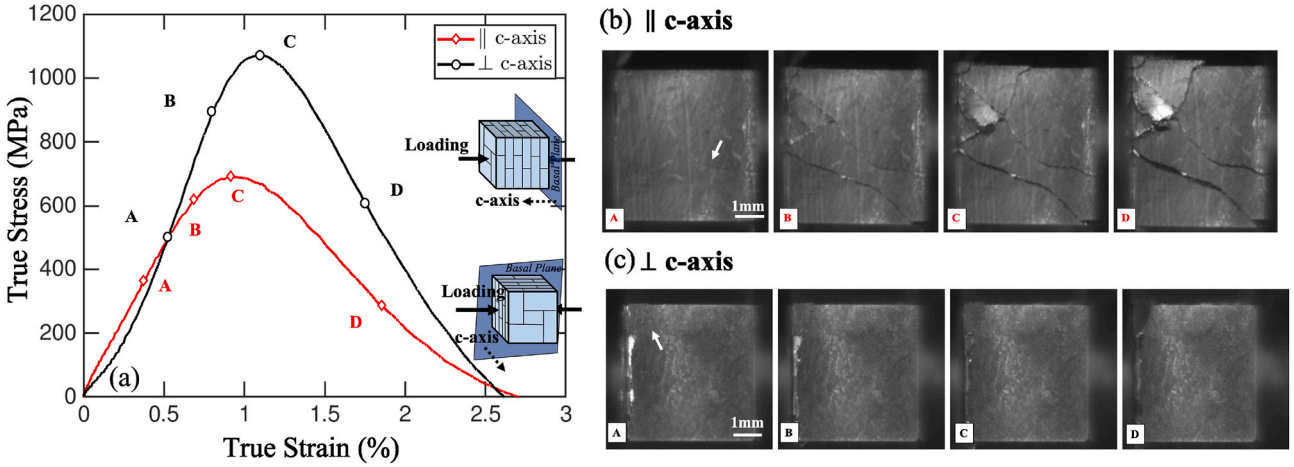

Fig. 8. Characteristic results of a ‖c-axis and ⊥c-axis loaded specimen under dynamic compression with representative ultra high-speed images on the right.

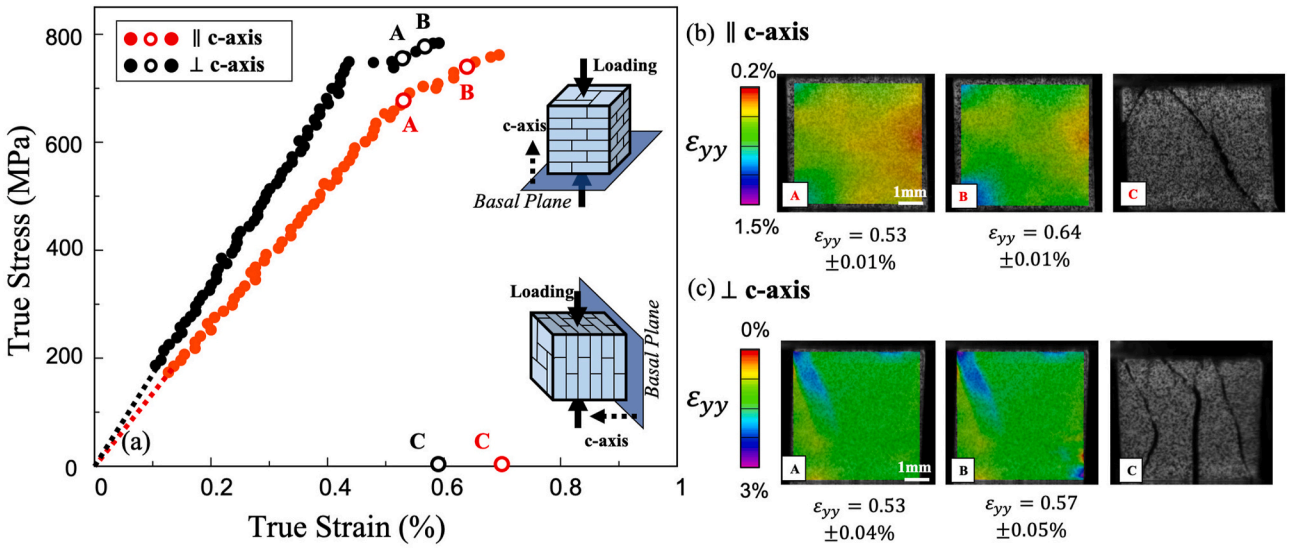

Fig. 9. Characteristic results of a ‖c-axis and ⊥c-axis loaded specimen under quasi-static compression with representative ultra high-speed images on the right. The plot presents strain starting from 0.1% (after the dashed lines) as a tow adjustment according to ASTM-E9 [61]. Representative average 2D DIC strain correlation results at the corresponding instants are shown where the axial strain is in the *y*, or vertical loading direction.

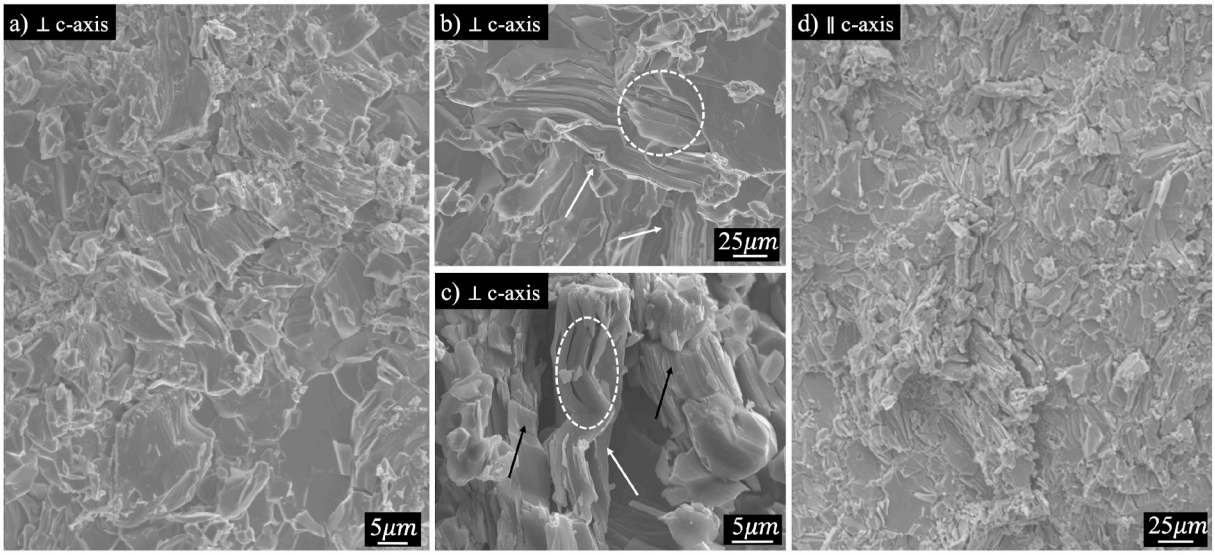

Fig. 10. SEM images of ⊥c-axis (a to c) and ‖c-axis (d) orientations after quasi-static loading in compression to failure. (a) Overall morphology of ⊥c-axis fracture surface. (b and c) ⊥c-axis surface at a higher magnification showing kink bands (white arrow), delamination (white dashed circle), intergranular (black arrow) and transgranular fracture/cleavage. (d) Overall morphology of a ‖c-axis surface shows mainly transgranular and some intergranular fracture.

quasi-static [12,20,25] compression experiments on other Ti-based MAX phases.

In comparison, the ⊥c-axis specimen exhibited a peak stress of 783 MPa, comparable to the ‖c-axis with only 2.5% difference, but the failure occurred at an earlier strain of 0.58%. Fig. 9(c) illustrates the representative images for three positions on the loading curve. This specimen is loaded along the basal plane with imaging performed on the non-basal plane, i.e. basal planes are stacked in-plane with each other. Shortly after the peak stress, Fig. 9(c) shows crack formation along the loading axis relatively parallel to the basal plane. Thus, the macroscopic fracture patterns revealed distinct forms in the two orientations examined.

3.3. Fractography

Fig. 10 shows the SEM micrographs of quasi-statically failed specimens. The overall morphology of the ⊥c-axis specimens exhibits cleavage suggesting that the crack propagates along the weaker grain boundaries. Fig. 10 (b) and (c) illustrate kink band formation (highlighted by the white arrows), delamination (highlighted by the white dashed circle), intergranular cracks (highlighted by black arrows) and transgranular cracks at higher magnification. These deformation mechanisms are similar to previously reported fracture morphologies on random oriented MAX phases [1,6,12]. The formation of kink bands suggest that basal planes underwent loading edge-on, causing kink band formation as previously reported in Refs. [8,11,22]. The evidence of kink bands and delaminations may explain the change in slope on the associated stress-strain curve near failure (point B on the black line of Fig. 9). However, the dominating cleavage/transgranular fracture imply an energy favorable crack path at a low strain rate, following intrinsic flaws along basal planes. When at low strain rates, internal defects and flaws nucleate cracks and enable the cracks to propagate along

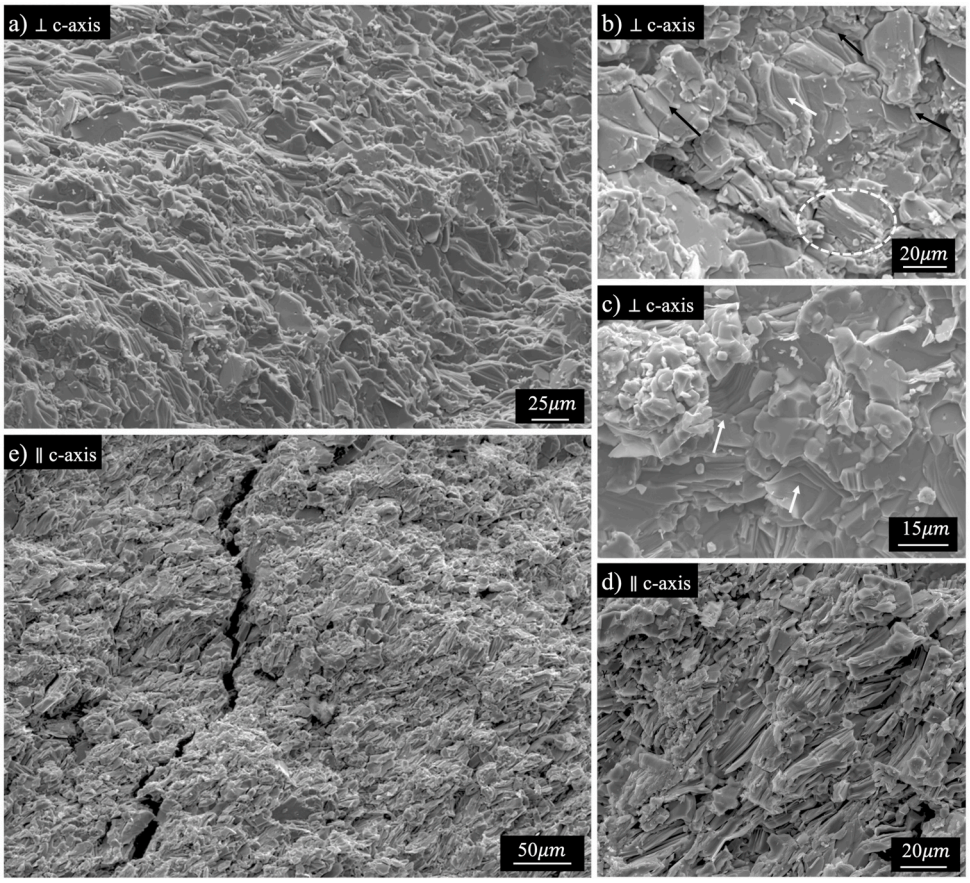

Fig. 11. SEM images of ⊥c-axis (a to c) and ‖c-axis (d to e) orientations after dynamic loading in compression to failure. (a) Overall morphology of ⊥c-axis fracture surface. (b and c) ⊥c-axis surface at a higher magnification with kink bands (white arrow), delaminations (white dashed circle), intergranular (black arrow) and transgranular fracture/cleavage shown. (d)‖c-axis fracture surface at higher magnification with a combination of transgranular and intergranular cracks. (e) Overall morphology of a ‖c-axis fracture surface with a clear running crack path.

energetically-favorable path, leading to the cleavage of the grain parallel to the basal plane. Fig. 10 (d) shows the overall morphology of a ‖c-axis fracture surface, where hardly any kink bands were observed, but where transgranular cracks and some intergranular cracks developed.

Fig. 11 shows the fracture behavior under dynamic conditions. The terrace morphology of ⊥c-axis in Fig. 11(a) indicates a layer by layer fracture at lower magnification. The terrace and wave-like morphology may help explain the prolonged strain at failure under dynamic loading where the subcritical crack propagation is exhibited, and the propagation of the internal microflaws is hindered by the inertial effects [62–64]. On higher magnification (as shown in Fig. 11 b and c), kink bands, delamination, intergranular cracks and transgranular/ cleavage cracks can be seen. Such observation indicates that kink band formation is active under dynamic loading and reasonable considering the time scale associated with dynamic deformation. Fig. 11(e) illustrates the fracture behavior of the ‖c-axis orientation. Fewer kinks are observed and no clear evidence of kink band formation was found. The overall morphology on the ‖c-axis orientation exhibits a combination of intergranular cracks and transgranular cracks, clearly indicated by the fractured grains and large crack path across the surface. These finding suggest that the higher compressive stress in ⊥c-axis could be due to a combination of kink bands, delamination, intergranular and transgranular cracking. The difference in dominant deformation and fracture mechanisms present in the fractographs between the two orientations suggest that additional microstructural tailoring may be possible to achieve even greater improvements in compressive strengths and strains at failure.

4. Conclusion

Textured bulk Ti_3SiC_2 was fabricated by sinter forging a 1:1:1.05 stoichiometric mixture of TiC, Si and Ti powders with a Lotgering factor of 0.87 on the c-axis orientation. The quasi-static and dynamic compressive responses, as well as hardness when loading parallel to the texture orientation, ‖c-axis, and perpendicular to the texture axis, ⊥c-axis, were evaluated. The ⊥c-axis orientation, where the basal planes are loaded edge-on, exhibited an average dynamic compressive strength of 987 MPa, 30% higher than the quasi-static loading at 761 MPa. However, the ‖c-axis orientation exhibited no discernible rate dependency on peak compressive strength. Both orientations exhibited an increase in strain at failure under dynamic loading on the order of 0.5%. Postmortem scanning electron microscopy revealed that the resulting fracture mechanisms on the ‖c-axis orientation appeared to be limited to intergranular cracks and transgranular cracks, and the imaging performed during loading showed macroscopic shear-like crack formation. Similar to structural ceramics, quasi-static loading appeared to have crack propagation more dominantly along the (potentially weaker) grain boundaries, but at higher loading rate, cracks increasingly divert to cleave the grain interior. The ⊥c-axis exhibited cracks forming along basal planes, creating delamination and kink bands even at the higher rate loading, which may help explain the improved strengths and fracture dissipation when compared with the ‖c-axis orientation.

Credit author statement

Xiangyuan Zhao: dynamic experimentation, Maxim Sokol: material fabrication, indentation andmicrostructure characterization, Michel Barsoum: supervision on material fabrication and microstructural characterization, data interpretation, Leslie Lamberson: supervision on dynamic characterization, data interpretation, All authors wrote parts of and edited manuscript.

Declaration of competing interest

The authors declare that they have no known competing financial interests or personal relationships that could have appeared to influence the work reported in this paper.

Acknowledgement

This research is supported by the CMMI division of the National Science Foundation under CAREER Grant No. 1939838 and Grant No. 1728041.

References

[1] M.W. Barsoum, MAX Phases: Properties of Machinable Ternary Carbides and Nitrides, Wiley-VCH, 2013.
[2] M. Sokol, V. Natu, S. Kota, M.W. Barsoum, On the chemical diversity of the MAX phases, Trends Chem. 1 (2) (2019) 210–223.
[3] M. Barsoum, T. El-Raghy, Synthesis and characterization of a remarkable ceramic: Ti_3SiC_2, J. Am. Ceram. Soc. 79 (7) (1996) 1953–1956.
[4] M.W. Barsoum, T. El-Raghy, The MAX phases: unique new carbide and nitride materials: ternary ceramics turn out to be surprisingly soft and machinable, yet also heat-tolerant, strong and lightweight, Am. Sci. 89 (4) (2001) 334–343.
[5] Z. Sun, Progress in research and development on MAX phases: a family of layered ternary compounds, Int. Mater. Rev. 56 (3) (2011) 143–166.
[6] M.W. Barsoum, M. Radovic, Elastic and mechanical properties of the MAX phases, Annu. Rev. Mater. Res. 41 (2011) 195–227.
[7] P. Eklund, M. Beckers, U. Jansson, H. Hogberg, L. Hultman, The $M_{n+1}AX_n$ phases: materials science and thin-film processing, Thin Solid Films 518 (8) (2010) 1851–1878.
[8] M.W. Barsoum, T. Zhen, S.R. Kalidindi, M. Radovic, A. Murugaiah, Fully reversible, dislocation-based compressive deformation of Ti_3SiC_2 to 1 GPa, Nat. Mater. 2 (2) (2003) 107–111.
[9] T. El-Raghy, M.W. Barsoum, A. Zavaliangos, S.R. Kalidindi, Processing and mechanical properties of Ti_3SiC_2: II, effect of grain size and deformation temperature, J. Am. Ceram. Soc. 82 (10) (1999) 2855–2860.
[10] M.F. Cover, O. Warschkow, M.M.M. Bilek, D.R. McKenzie, A comprehensive survey of M_2AX phase elastic properties, J. Phys. Condens. Matter 21 (30) (2009) 305–403.
[11] M.W. Barsoum, L. Farber, T. El-Raghy, Dislocations, kink bands, and room-temperature plasticity of Ti_3SiC_2, Metall. Mater. Trans. 30 (7) (1999) 1727–1738.
[12] M. Barsoum, T. El-Raghy, Room-temperature ductile carbides, Metall. Mater. Trans. 30 (2) (1999) 363–369.
[13] A. Kushima, X. Qian, P. Zhao, S. Zhang, J. Li, Ripplocations in van der Waals layers, Nano Lett. 15 (2) (2015) 1302–1308.
[14] J. Griggs, A.C. Lang, J. Gruber, G. Tucker, M. Taheri, M. Barsoum, Spherical nanoindentation, modeling and transmission electron microscopy evidence for ripplocations in Ti_3SiC_2, Acta Mater. 131 (2017) 141–155.
[15] M. Barsoum, G. Tucker, Deformation of layered solids: ripplocations not basal dislocations, Scripta Mater. 139 (2017) 166–172.
[16] J. Gruber, A.C. Lang, J. Griggs, M.L. Taheri, G.J. Tucker, M.W. Barsoum, Evidence for bulk ripplocations in layered solids, Sci. Rep. 6 (2016) 33451.
[17] M.W. Barsoum, X. Zhao, S. Shanazarov, A. Romanchuk, S. Koumlis, S.J. Pagano, L. Lamberson, G.J. Tucker, Ripplocations: a universal deformation mechanism in layered solids, Phys. Rev. Mater. 3 (2018), 013602.
[18] C. Brüsewitz, I. Knorr, H. Hofsäss, M.W. Barsoum, C.A. Volkert, Single crystal pillar microcompression tests of the MAX phases Ti_2InC and Ti_4AlN_3, Scripta Mater. 69 (4) (2013) 303–306.
[19] Z. Zhang, Z. Sun, Shear fracture behavior of Ti_3SiC_2 induced by compression at temperatures below 1000C, Mater. Sci. Eng., A 408 (1–2) (2005) 64–71.
[20] B. Poon, L. Ponson, J. Zhao, G. Ravichandran, Damage accumulation and hysteretic behavior of MAX phase materials, J. Mech. Phys. Solid. 59 (10) (2011) 2238–2257.
[21] N. Jones, C. Humphrey, L. Connor, O. Wilhelmsson, L. Hultman, H. Stone, F. Giuliani, W. Clegg, On the relevance of kinking to reversible hysteresis in MAX phases, Acta Mater. 69 (2014) 149–161.
[22] A.G. Zhou, M.W. Barsoum, Kinking nonlinear elastic deformation of Ti_3AlC_2, Ti_2AlC, $Ti_3Al(C_{0.5},N_{0.5})_2$ and $Ti_2Al(C_{0.5},N_{0.5})$, J. Alloys Compd. 498 (1) (2010) 62–70.
[23] M.W. Barsoum, T. Zhen, A. Zhou, S. Basu, S.R. Kalidindi, Microscale modeling of kinking nonlinear elastic solids, Phys. Rev. B 71 (13) (2005) 134101.
[24] S. Kalidindi, T. Zhen, M. Barsoum, Macroscale constitutive modeling of kinking nonlinear elastic solids, Mater. Sci. Eng., A 418 (1–2) (2006) 95–98.
[25] N.V. Tzenov, M.W. Barsoum, Synthesis and characterization of Ti_3SiC_2, J. Am. Ceram. Soc. 83 (4) (2000) 825.
[26] C. Hu, H. Zhang, F. Li, Q. Huang, Y. Bao, New phases' discovery in MAX family, Int. J. Refract. Metals Hard Mater. 36 (2013) 300–312.
[27] G. Messing, S. Poterala, Y. Chang, T. Frueh, E. Kupp, B. Watson, R. Walton, M. Brova, A. Hofer, R. Bermejo, R. Meyer, Texture-engineered ceramics-property enhancements through crystallographic tailoring, J. Mater. Res. 32 (17) (2017) 3219–3241.
[28] X. Chen, G. Bei, Toughening mechanisms in nanolayered MAX phase ceramics-A review, Materials 10 (4) (2017) 366.
[29] F. Lotgering, Topotactical reactions with ferrimagnetic oxides having hexagonal crystal structures—I, J. Inorg. Nucl. Chem. 9 (2) (1959) 113–123.
[30] X. Zhu, Y. Sakka, Textured silicon nitride: processing and anisotropic properties, Sci. Technol. Adv. Mater. 9 (3) (2008), 033001.
[31] X. Duan, L. Shen, D. Jia, Y. Zhou, S. van der Zwaag, W.G. Sloof, Synthesis of high-purity, isotropic or textured Cr_2AlC bulk ceramics by spark plasma sintering of pressure-less sintered powders, J. Eur. Ceram. Soc. 35 (5) (2015) 1393–1400.
[32] C. Hu, Y. Sakka, T. Nishimura, S. Guo, S. Grasso, H. Tanaka, Physical and mechanical properties of highly textured polycrystalline Nb_4AlC_3 ceramic, Sci. Technol. Adv. Mater. 12 (4) (2011), 044603.
[33] C. Hu, Y. Sakka, H. Tanaka, T. Nishimura, S. Grasso, Fabrication of textured Nb_4AlC_3 ceramic by slip casting in a strong magnetic field and spark plasma sintering, J. Am. Ceram. Soc. 94 (2) (2011) 410–415.
[34] C. Hu, Y. Sakka, S. Grasso, T. Nishimura, S. Guo, H. Tanaka, Shell-like nanolayered Nb_4AlC_3 ceramic with high strength and toughness, Scripta Mater. 64 (8) (2011) 765–768.
[35] M. Shamma, E.N. Caspi, B. Anasori, B. Clausen, D.W. Brown, S.C. Vogel, V. Presser, S. Amini, O. Yeheskel, M.W. Barsoum, In situ neutron diffraction evidence for fully reversible dislocation motion in highly textured polycrystalline Ti_2AlC samples, Acta Mater. 98 (2015) 51–63.
[36] T. Lapauw, K. Vanmeensel, K. Lambrinou, J. Vleugels, A new method to texture dense $M_{n+1}AX_n$ ceramics by spark plasma deformation, Scripta Mater. 111 (2016) 98–101.
[37] Y. Liu, F. Li, Y. Li, H. Cui, Y. Pu, S. Guo, Z. Shi, Highly textured Ti_2AlN ceramic prepared via thermal explosion followed by edge-free spark plasma sintering, Scripta Mater. 136 (2017) 55–58.
[38] Y. Mizuno, K. Sato, M. Mrinalini, T.S. Suzuki, Y. Sakka, Fabrication of textured Ti_3SiC_2 by spark plasma sintering and their anisotropic mechanical properties, J. Ceram. Soc. Jpn. 121 (1412) (2013) 366–369.
[39] L. Xu, D. Zhu, S. Grasso, T.S. Suzuki, A. Kasahara, M. Tosa, B.-n. Kim, Y. Sakka, M. Zhu, C. Hu, Effect of texture microstructure on tribological properties of tailored Ti_3AlC_2 ceramic, J. Adv. Ceram. 6 (2) (2017) 120–128.
[40] H.B. Zhang, C.F. Hu, K. Sato, S. Grasso, M. Estili, S.Q. Guo, K. Morita, H. Yoshida, T. Nishimura, T.S. Suzuki, M.W. Barsoum, B.N. Kim, Y. Sakka, Tailoring Ti_3AlC_2 ceramic with high anisotropic physical and mechanical properties, J. Eur. Ceram. Soc. 35 (1) (2015) 393–397.
[41] C. Hu, Y. Sakka, S. Grasso, T. Suzuki, H. Tanaka, Tailoring Ti_3SiC_2 ceramic via a strong magnetic field alignment method followed by spark plasma sintering, J. Am. Ceram. Soc. 94 (3) (2011) 742–748.
[42] K. Sato, M. Mishra, H. Hirano, T. Suzuki, Y. Sakka, Fabrication of textured Ti_3SiC_2 ceramic by slip casting in a strong magnetic field and pressureless sintering, J. Ceram. Soc. Jpn. 122 (1429) (2014) 817–821.
[43] M. Mishra, Y. Sakka, C. Hu, T.S. Suzuki, T. Uchikoshi, L. Besra, Y. Zhou, Electrophoretic deposition of Ti_3SiC_2 and texture development in a strong magnetic field, J. Am. Ceram. Soc. 95 (9) (2012) 2857–2862.
[44] L. Shannahan, M.W. Barsoum, L. Lamberson, Dynamic fracture behavior of a MAX phase Ti^3SiC_2, Eng. Fract. Mech. 169 (2017) 54–66.
[45] D. Clarkin, Dynamic Response of Ti_2AlC under Radial Confinement at High Temperature, Ph.D. thesis, University of Rhode Island, 2017.
[46] R. Bhattacharya, R. Benitez, M. Radovic, N.C. Goulbourne, High strain-rate response and deformation mechanisms in polycrystalline Ti_2AlC, Mater. Sci. Eng., A 598 (2014) 319–326.
[47] P. Naik Parrikar, R. Benitez, H. Gao, M. Radovic, A. Shukla, The effect of grain size on deformation and failure of Ti_2AlC MAX phase under thermo-mechanical loading, Exp. Mech. 57 (5) (2017) 675.
[48] P. Naik Parrikar, R. Benitez, H. Gao, M. Radovic, A. Shukla, Mechanical response of fine grained Ti_2AlC under extreme thermo-mechanical loading conditions, Mater. Sci. Eng., A 658 (2016) 176–184.
[49] M. Sokol, S. Kalabukhov, E. Zaretsky, M.W. Barsoum, Abnormal response of Ti_3SiC_2 to high strain-rate loading, Phys. Rev. Mater. 3 (6) (2019), 063610.
[50] C.A. Schneider, W.S. Rasband, K.W. Eliceiri, NIH Image to ImageJ: 25 years of image analysis, Nat. Methods 9 (7) (2012) 671.
[51] S. Yaofeng, J.H. Pang, Study of optimal subset size in digital image correlation of speckle pattern images, Optic Laser. Eng. 45 (9) (2007) 967–974.
[52] M.A. Sutton, J.J. Orteu, H. Schreier, Image Correlation for Shape, Motion and Deformation Measurements: Basic concepts, in: Theory and Applications, Springer Science & Business Media, 2009.
[53] S. Koumlis, S. Pagano, G. Retuerta del Rey, Y. Kim, P. Jewell, M. Noh, L. Lamberson, Drop on demand colloidal suspension inkjet patterning for DIC, Exp. Tech. 43 (2) (2019) 137–148.
[54] H. Kolsky, An investigation of the mechanical properties of materials at very high rates of loading, Proc. Phys. Soc. B 62 (11) (1949) 676–700.
[55] S. Sarva, S. Nemat-Nasser, Dynamic compressive strength of silicon carbide under uniaxial compression, Mater. Sci. Eng., A 317 (1) (2001) 140–144.
[56] K.T. Ramesh, in: High Strain Rate and Impact Experiments, vol. 1, Springer Handbook of Experimental Solid Mechanics, 2008.
[57] G. Hu, K. Ramesh, B. Cao, J. McCauley, The compressive failure of aluminum nitride considered as a model advanced ceramic, J. Mech. Phys. Solid. 59 (5) (2011) 1076–1093.
[58] Z. Wang, R. Li, W. Song, Dynamic failure and inelastic deformation behavior of SiC ceramic under uniaxial compression, Ceram. Int. 46 (1) (2020) 612–617.
[59] Z. Huang, Z. Pan, H. Li, Q. Wei, X. Li, Hidden energy dissipation mechanism in nacre, J. Mater. Res. 29 (14) (2014) 1573–1578.
[60] P. Lava, D. Debruyne, MatchID (2010).
[61] I. ASTM, in: Standard Test Methods of Compression Testing of Metallic Materials at Room Temperature, vol. 19, ASTM E9, 2019.

[62] H. Wang, K. Ramesh, Dynamic strength and fragmentation of hot-pressed silicon carbide under uniaxial compression, Acta Mater. 52 (2004) 355–367.
[63] J. Lankford, Compressive failure of fibre-reinforced composites: buckling, kinking, and the role of the interphase, J. Mater. Sci. 30 (1995) 4343–4348.
[64] G. Ravichandran, G. Subhash, A micromechanical model for high strain rate behavior of ceramics, Int. J. Solid Struct. 32 (17) (1995) 2626–2646.